(2)

Naval Research Laboratory
Washington, DC 20375-5000

NRL Memorandum Report 6690

Numerical Simulation of the Compressible Orszag-Tang Vortex II. Supersonic Flow

J. M. PICONE AND R. B. DAHLBURG

Laboratory for Computational Physics and Fluid Dynamics

August 5, 1990

Approved for public release; distribution unlimited.

REPORT DOCUMENTATION PAGE	*Form Approved* *OMB No. 0704-0188*

1. AGENCY USE ONLY *(Leave blank)*

2. REPORT DATE 1990 August 5

3. REPORT TYPE AND DATES COVERED Interim

4. TITLE AND SUBTITLE

Numerical Simulation of the Compressible
Orszag-Tang Vortex II. Supersonic Flow

5. FUNDING NUMBERS

PE - W-16, 672
PR - W-16m672
TA - NASA

6. AUTHOR(S)

J. Michael Picone and Russell B. Dahlburg

7. PERFORMING ORGANIZATION NAME(S) AND ADDRESS(ES)

Naval Research Laboratory
Washington, DC 20375-5000

8. PERFORMING ORGANIZATION REPORT NUMBER

NRL Memorandum
Report 6690

9. SPONSORING/MONITORING AGENCY NAME(S) AND ADDRESS(ES)

Office of Naval Research
800 N. Quincy St.
Arlington, VA 22217-5999

National Aeronautics
Washington, DC 20546

10. SPONSORING/MONITORING AGENCY REPORT NUMBER

11. SUPPLEMENTARY NOTES

12a. DISTRIBUTION/AVAILABILITY STATEMENT

Approved for public release; distribution unlimited.

12b. DISTRIBUTION CODE

13. ABSTRACT *(Maximum 200 words)*

→ Tang beta

We continue our numerical investigation of the Orszag-Tang vortex system in compressible magnetofluids ~~by~~ considering initial conditions with embedded supersonic regions. The simulations have initial average Mach numbers $M = 1.0$ and 1.5 and $\beta = 10/3$ with Lundquist numbers $S = 50$, 100, or 200. The behavior of the system differs significantly from that found previously for the incompressible and subsonic analogs. Shocks form at the downstream boundaries of the embedded supersonic regions outside the central magnetic X-point and produce strong local current sheets which dissipate appreciable magnetic energy. Reconnection at the central X-point, which dominates the incompressible and subsonic systems, peaks later and has a smaller impact as M increases from 0.6 to 1.5. Similarly, correlation between the momentum and magnetic field begins significant growth later than in subsonic and incompressible flows. The shocks bound large compression regions, which dominate the wavenumber spectra of autocorrelations in mass density, velocity, and magnetic field.

14. SUBJECT TERMS

Compressible magnetohydrodynamic turbulence, solar wind structuring, Direct numerical simulation,

15. NUMBER OF PAGES 45

16. PRICE CODE

17. SECURITY CLASSIFICATION OF REPORT	18. SECURITY CLASSIFICATION OF THIS PAGE	19. SECURITY CLASSIFICATION OF ABSTRACT	20. LIMITATION OF ABSTRACT
UNCLASSIFIED	UNCLASSIFIED	UNCLASSIFIED	UL

NSN 7540-01-280-5500

Standard Form 298 (Rev 2-89)
Prescribed by ANSI Std Z39-18
298-102

CONTENTS

NUMERICAL SIMULATION OF THE COMPRESSIBLE ORSZAG-TANG VORTEX II. SUPERSONIC FLOW

I. INTRODUCTION

In a recent paper, to be designated as I [1], we initiated a systematic research program using numerical simulations of dissipative, fully compressible magnetofluids to identify and analyze the effects of compressibility on magnetohydrodynamic (MHD) turbulence. The first studies, reported therein, tracked the decay of initially subsonic flow fields and used the analogous incompressible flows as baselines for comparison. The initial average Mach number M ranged from 0.2 to 0.6, and the ratio of thermal to magnetic pressure (β) ranged from 30.0 to 10/3. The initial, dimensionless mass density was uniform at $\rho = 1$ while the Lundquist numbers varied from 50 to 200.

The present paper deals with the effect of embedded supersonic flows and the resulting emerging shock waves on phenomena associated with MHD turbulence, including reconnection, the formation of current sheets and vortex structures, and the evolution of spatial and temporal correlations among physical variables. The parameters used here are $M = 1.0$ and 1.5, $\rho = 2.78$ and 6.25, respectively, and $\beta = 10/3$, with the same range of Lundquist numbers as above. Often flows within regions bounded by shocks are locally subsonic, and the previous subsonic calculations should apply to those regions. However, both the supersonic disturbances responsible for forming the shocks and the current sheets accompanying the shocks will have effects on the overall flow field which cannot be predicted on the basis of the subsonic studies alone. An example is the production of turbulence by inhomogeneous laser pulses propagating in a gas [2, 3]. The laser pulse produces a channel in the background gas, with some regions of the channel cross section heated more than others. The resulting shocks interact with the inhomogeneous density distribution of the channel to produce turbulence. This paper provides initial descriptions and assessments of similar supersonic effects upon a compressible magnetofluid. Our results should be useful in describing local supersonic regions in a turbulent, compressible, dissipative magnetofluid.

Among the obvious complicating factors in fully compressible MHD flows are density and entropy fluctuations, finite magnetoacoustic waves, discontinuities (e.g., shocks and

---

Manuscript approved June 4, 1990.

contact surfaces), and a finite information transport velocity. Theories of "weakly compressible" MHD flows [4, 5, 6, 7], while both useful and elegant, account only for density fluctuations (and not entropy fluctuations), filtering acoustic waves out of the solution or damping them out on a rapid time scale. To reveal the full range of compressible, turbulent phenomena, initial studies must necessarily survey the phenomenology of relevant nonisentropic flows which include all of the effects mentioned at the beginning of this paragraph. One can then begin to identify problems requiring theoretical treatment and exhaustive numerical study using the maximum achievable resolution.

Our approach differs from that of many other studies of turbulence in that we have chosen a model problem, the Orszag-Tang vortex system [8], which involves decay from nonrandom initial conditions, rather than to follow the decay of a random initial field or the evolution of a driven turbulent flow. The Orszag-Tang system is doubly periodic, and the initial conditions consist of single-mode, solenoidal velocity and magnetic fields, each containing X-points and O-points. The initial mass density is flat and the initial pressure fluctuations are incompressible, balancing the local forces for a magnetofluid of unit mass density. The identification and tracking of the various compressible MHD phenomena thus are more straightforward than in a statistical approach. In addition, such a simple, easily reproducible, model problem can serve as a useful reference for comparison with the results from studies of more realistic turbulent fields [9]. This model problem, in fact, contains most of the significant features of MHD turbulence, including dissipation of magnetic and kinetic energy, reconnection, formation of high-density jets, selective decay, dynamic alignment, and the emergence and manifestations of small-scale structure. The incompressible version has received thorough study [10] and provides an excellent baseline for direct quantitative and structural comparisons with the evolution in a compressible medium. Past treatments also have emphasized the relationship of the Orszag-Tang vortex system to the theory of resistive tearing modes [11]. Similar highly resolved compressible calculations should be performed for various magnetoacoustic Mach numbers and values of plasma β. The popularity and simplicity of the model also make it an obvious choice for comparison and calibration of numerical algorithms for simulating compressible MHD turbulence.

Our previous paper [1] has added subsonic flow as another useful baseline for studies of supersonic flows. That paper provides a background on the relevant literature and a detailed discussion of various formulations and numerical methods used for compressible MHD turbulence and associated phenomena. The present paper deals with situations in which regions of appreciable supersonic flow lead to the emergence of shocks. These flows have a major effect on reconnection at the X-points in the magnetic field, the density jets originally observed at subsonic Mach numbers, the formation of other density extrema, the dissipation of energy through the formation of current sheets at the shocks, and the spectral composition of autocorrelations and cross-correlations of physical variables. The next section describes briefly our formulation and numerical methods. Section III presents our results on the evolution of the local structure of the flow field, the global properties of the system, and spectral correlations. Section IV discusses the important dynamical properties and observational consequences of embedded supersonic regions and emerging shocks in the Orszag-Tang model of an MHD system undergoing reconnection. We also draw conclusions regarding the effects of local supersonic regions on MHD turbulence.

II. NUMERICAL SIMULATIONS

A. Formulation

The following nonlinear partial differential equations, written in dimensionless form, govern the behavior of a two-dimensional, compressible, dissipative magnetofluid in our numerical simulations:

$$\frac{\partial \rho}{\partial t} = -\nabla \cdot (\rho \mathbf{v}) , \tag{1a}$$

$$\frac{\partial\,(\rho \mathbf{v})}{\partial t} = -\nabla \cdot \left[\rho \mathbf{v}\mathbf{v} - \mathbf{B}\mathbf{B} + \frac{1}{2}(p + |\mathbf{B}|^2)\mathbf{I} - \frac{1}{S_v}\tau\right] , \tag{1b}$$

$$\frac{\partial \mathbf{B}}{\partial t} = \nabla \times \left[\mathbf{v} \times \mathbf{B} - \frac{1}{S_r}\nabla \times \mathbf{B}\right] , \tag{1c}$$

$$\begin{aligned}\frac{\partial E}{\partial t} = -\nabla \cdot \Big[&(E + p)\mathbf{v} + (|\mathbf{B}|^2\mathbf{I} - 2\mathbf{B}\mathbf{B}) \cdot \mathbf{v} \\ &- \frac{2}{S_v}\mathbf{v} \cdot \tau + \frac{2}{S_r}(\mathbf{B} \cdot \nabla\mathbf{B} - \nabla\mathbf{B} \cdot \mathbf{B}) \\ &- \frac{\gamma}{\gamma - 1}\,\frac{1}{S_v\,Pr}\nabla T\Big],\end{aligned} \tag{1d}$$

$$\nabla \cdot \mathbf{B} = 0 , \tag{1e}$$

with an equation of state,

$$p = (\gamma - 1)U \ . \tag{2}$$

Here ρ is the mass density, $\mathbf{v}$ is the flow velocity, p is the mechanical pressure, $\mathbf{I}$ is the unit dyad, $\mathbf{B}$ is the magnetic induction field, U is the internal energy density, E is the total energy density, given in dimensionless units by

$$E(\mathbf{x}, t) \equiv \rho|\mathbf{v}|^2 + |\mathbf{B}|^2 + U, \tag{3}$$

$T \equiv p/\rho$ is the dimensionless temperature, $\tau \equiv \left[(\partial_j v_i + \partial_i v_j) - \frac{2}{3}\nabla \cdot \mathbf{v}\delta_{ij}\right] \hat{\mathbf{e}}_i\ \hat{\mathbf{e}}_j$ is the stress tensor, and $\gamma \equiv 5/3$ is the ratio of specific heats. The thermal conductivity (κ), magnetic resistivity (η), and viscosity (μ) are constant and uniform, and we have assumed that the bulk viscosity is zero [12]. Important dimensionless numbers are the viscous Lundquist number $S_v \equiv \rho_0 V_A^0 L_0/\mu$ [13], the resistive Lundquist number $S_r = V_A^0 L_0/\eta$, and the Prandtl number $Pr = c_p\mu/\kappa$.

In these definitions, ρ_0 is a characteristic density, V_A^0 is a characteristic Alfvén speed, L_0 is a characteristic length equal to the reciprocal of the minimum wavenumber $k_{\min} = 2\pi/L$ ($L =$ system length), c_p is the specific heat at constant pressure, and $V_0 = V_A^0$ is a characteristic flow speed. The thermodynamic normalization sets

$$E_0 = p_0 = B_0^2/8\pi = \rho_0 {V_A^0}^2/2 \quad . \tag{4}$$

Time (t) is measured in units of the Alfvén transit time L_0/V_A^0. For the runs reported here, we set $S_v = S_r = 50,\ 100,$ or 200 and $Pr = 1$. All of our numerical simulations assume unit magnetic Prandtl number, *i.e.*, $\mu/(\rho_0\eta) = 1$, so we subsequently consider only the parameter $S = S_v = S_r$.

B. Initial Conditions

The initial magnetic and velocity fields are identical to the vortex system of Orszag and Tang (1979):

$$\rho(x, y, t = 0) = \text{constant} \equiv \rho^0, \tag{6a}$$

$$\mathbf{v}(x, y, t = 0) = -\sin y\ \hat{\mathbf{e}}_x + \sin x\ \hat{\mathbf{e}}_y, \tag{6b}$$

and

$$\mathbf{B}(x, y, t = 0) = -\sin y\ \hat{\mathbf{e}}_x + \sin 2x\ \hat{\mathbf{e}}_y, \tag{6c}$$

where $\hat{e}_x$ and $\hat{\mathbf{e}}_y$ are unit vectors in the x and y directions respectively. For reasons given below, our investigations of emerging shocks use an initial mass density which can differ from unity. The initial cross helicity and normalized correlation between the velocity and magnetic fields then equal 0.5. As in our previous calculations, the initial mechanical pressure, $p(t = 0)$, comprises a mean part, $\langle p(t = 0)\rangle \equiv p^0$, and a fluctuating part, $\delta p(x, y, t = 0) \equiv \delta p^0(x, y)$. Here the bracket notation represents a volume average, *i.e.*, an average of a function (f) over the entire grid ($\mathcal{G}$):

$$\langle f\rangle = \frac{\int\limits_{\mathcal{G}} f(x,y,t)\;dx\;dy}{\int\limits_{\mathcal{G}} dx\;dy} \quad . \tag{7}$$

The equation for the dimensionless speed of sound,

$$C_S^2 = \frac{\gamma p}{2\rho} \quad , \tag{8}$$

constrains the total pressure to equal or exceed zero. The lower bound on p^0 is then a positive definite functional of $\delta p^0(x, y)$, given by $p^0_{\min} \geq \max\{-\,\delta p^0\}$, assuming that the choice of δp^0 is not identically zero in the computational domain.

Equation (8) indicates that formula for the local Mach number $\mathcal{M}$ is

$$\mathcal{M}^2 = \frac{2\rho|\mathbf{v}|^2}{\gamma\, p} \quad . \tag{9a}$$

Notice that the pressure must be greater than zero everywhere in order for $\mathcal{M}$ to be real and free of singularities throughout the grid. To obtain a "characteristic" or an "average" Mach number M at time $t = 0$ for the flows in our calculations, we substitute $\rho = \rho^0$, $p = p^0$, and $|\mathbf{v}^0| = \sqrt{\langle \mathbf{v}^2(t = 0)\rangle}$ into Eq.(9a):

$$M^2 = \frac{2\rho^0|\mathbf{v}^0|^2}{\gamma\, p^0} \quad . \tag{9b}$$

The ratio of thermal to magnetic pressure depends on local Mach number according to

$$\beta \equiv \frac{p}{|\mathbf{B}|^2} = \frac{2\rho|\mathbf{v}|^2}{\gamma\mathcal{M}^2|\mathbf{B}|^2} \quad . \tag{10}$$

In all calculations, the initial "characteristic" value, β_c, is 10/3, to permit comparison with the $M = 0.6$ case considered previously [1]. The quantity β_c relates to β in Eq.(10) as M does to $\mathcal{M}$.

Equation (9a) shows that one could obtain flows with supersonic regions merely by setting the initial background pressure p^0 close enough in magnitude to the minimum (negative) value of the fluctuating pressure δp^0. As in our subsonic calculations, δp^0 would be the solution of the incompressible MHD equations with $\rho^0 = 1$. Unfortunately as $p^0 \rightarrow \max\{-\delta p^0\}$, the supersonic regions move inward toward the center of the grid, which is a stagnation point of the flow and an X-point of the magnetic field. Figure 1(a) shows the initial local Mach number $\mathcal{M}$ when the minimum value of the thermal pressure is 10^{-4}. The average background pressure is $p^0 \approx 2.6$, making $M \approx 0.679$. The initial maximum value of $\mathcal{M}$ is approximately 2.2, since the minimum pressure occurs near the stagnation point. Calculation of this case up to $t = 8$ shows only small differences from the $M = 0.6$ subsonic case studied previously, even though the latter had an initial maximum value of 0.97 for $\mathcal{M}$. In fact, both calculations exhibit supersonic flows early, but no shocks occur [1]. Erlebacher *et al.* have reported a similar result for 3-D, compressible, Navier-Stokes turbulence [14].

For the study of effects related to emerging shocks within this model, another prescription is necessary. Our approach is to increase ρ^0 above 1.0 while retaining the definitions of $\mathbf{v}^0$ and $\mathbf{B}^0$ in Eqs.(6b) and (6c). In addition, we allow the fluctuating pressure, δp^0, to satisfy the incompressible equation of motion *with* ρ^0 *set equal to one.* With the proper choice of p^0, we can define a set of initial conditions which are the same as those of the previous subsonic study except for the initial mass density. By increasing ρ^0, we can raise the characteristic Mach number (Eq.(9b)) of the flow above 1.0. Since these choices of ρ^0 and δp^0

do not satisfy the incompressible equation of motion, an imbalance exists between the momentum gradients of the fluid and the opposing magnetic and thermal pressure fields. This imbalance, in fact, causes the supersonic disturbances which we desire to study. In support of this approach, Appendix A shows that attempting to maintain a balance among local forces confines us to subsonic characteristic Mach numbers $M \leq 0.679$, if the amplitudes of the velocity and magnetic field fluctuations are equal, as in Eq.(6).

Our choice of initial average pressure p^0 is 10/3, and the corresponding characteristic β_c is also 10/3. These values are the same as in the $M = 0.6$ subsonic calculation [1], in which $\rho^0 = 1$. The present calculations, therefore, are linked directly to our previous work. To ensure that significant supersonic regions are present, we set the characteristic Mach number $M \geq 1$, giving an initial mass density $\rho^0 \geq 2.78$ by Eq.(9b). Here we calculate the system evolution for $M = 1.0$, $\rho^0 = 2.78$, and $M = 1.5$, $\rho^0 = 6.25$. Figure 1(b) shows the initial form of the local Mach number, $\mathcal{M}$, for the $M = 1.0$ calculation. The local Mach number varies widely over the system from a value of 0.0 at the stagnation point in the center of the computational grid to a value of 1.6 within sizable supersonic regions. Section III shows that these regions produce shocks which alter the evolution significantly from the subsonic and incompressible baselines.

C. Numerical Algorithm

Previous papers have described our numerical algorithm in detail [1, 15]. Our code, *CRUNCH2D*, implements a Fourier collocation method and employs an isotropic truncation in Fourier space at each time-level [14]. The modified Euler method, a second-order Runge-Kutta scheme [16], discretizes time. The time step, Δt, is limited by a compressible MHD Courant-Friedrichs-Lewy (CFL) number,

$$\mathcal{N}_{CFL} \;=\; \sup\left\{\frac{(|\mathbf{v}| + C_S + V_A)\Delta t}{h}\right\} \;\leq\; 0.3 \;, \qquad (11)$$

where C_S = sound speed and $h = 2\pi/N = \Delta x = \Delta y$. When shocks are present, reduction in the time step according to Eq.(11) (as compared to subsonic flows) often is insufficient to guarantee a smooth solution in the vicinity of the shock. In such situations, the thermal pressure and the mass density can have local negative values, and increased viscous and resistive dissipation often are necessary. When the diffusive terms are considered separately, numerical instability can occur due to enhanced transport in the vicinity of the shock discontinuity. We have, therefore, added stability criteria based on viscous dissipation [17] and resistive dissipation, respectively:

$$\begin{aligned} \mathcal{N}_v &= \frac{N^2\Delta t}{4S_v\rho_{\min}} \leq 1 \\ \mathcal{N}_r &= \frac{N^2\Delta t}{4S_r} \leq 1 \end{aligned} \quad . \tag{12}$$

Our simulations consume approximately 17 μs per time step per grid point on a single processor of the Numerical Aerodynamic Simulation Program (NAS) Cray Y-MP computer at the NASA Ames Research Center. For $M = 1$ and Lundquist numbers $S = 50$, we use 256^2 collocation points while for $M = 1$, $S \geq 100$, and $M = 1.5$, $S = 50$, we use 512^2 collocation points. The calculations with 512^2 collocation points require approximately 7 million words of core memory. With these dissipation levels and resolutions, CRUNCH2D can simulate processes with moderate strength shocks ($\mathcal{M} \leq 3.0$), as verified by a number of standard tests, e.g., the rupturing diaphragm problem [15] and the numerical simulations in I. Our model shocks are approximately 5 computational cells thick when $S = 200$ and $N = 256^2$ [15].

III. RESULTS AND DISCUSSION

As in our previous paper [1], our investigation of compressibility in the Orszag-Tang vortex model relies primarily on such diagnostics as time-dependent area integrals, contour diagrams, generalized streamline plots, and wavenumber spectra of various autocorrelations and cross correlations. The reader should refer to that paper for the corresponding plots when M ranges from 0.2 to 0.6. Supersonic compression and the presence of shocks profoundly influence energy dissipation, the time at which the onset of strong reconnection occurs at the magnetic X-point, the longevity of reconnection and the associated current sheet, and the evolution and extent of the correlation between the magnetic and velocity fields. The wavenumber spectra and the evolution of global averages thus differ significantly from those of subsonic flows. To aid in the interpretation of those differences, the discussion begins with structural features.

A. Structural Effects of Supersonic Flows and Emerging Shocks

For the incompressible and subsonic systems, the structures of interest are those associated with magnetic field reconnection: magnetic islands and their coalescence, jets emerging from the reconnection zone, vortex quadrupoles, and electric current sheets ("reconnection current sheets" or RCS). In the supersonic cases discussed below, shocks and their associated current sheets ("shock current sheets" or SCS) and distributions of vorticity and dilatation ($\nabla \cdot \mathbf{v}$) constitute additional structural features which become dominant as Mach number increases. Since the system is decaying with time, the most interesting structural effects occur for times $t \leq 4.0$. Most of the results presented in this subsection, therefore, correspond to that temporal range.

An additional process emerges due to the self-interaction of the magnetofluid via shock wave propagation through the system. Because of the symmetry and periodicity of the Orszag-Tang model, the shocks (and later, finite acoustic waves) can interact multiple times with each other and with the spatially varying mass density field. The latter interactions generate progressively smaller-scale vortex structures and density fluctuations, and can cause the magnetofluid to appear turbulent at later times [1, 18, 19]. Picone *et al.* [20] have provided a simple numerical demonstration of this phenomenon. The newly generated vorticity affects the local mass density on time scales corresponding to the induced rotational motion rather than the shock transit. Thus the readily detectable manifestations appear gradually and with temporally increasing prominence.

To illustrate the shock-emergence process, we follow the time development of the local Mach number $\mathcal{M}$ throughout the grid. Figure 2 shows the evolution of $\mathcal{M}$ for the calculation in which the average initial Mach number $M = 1.0$ and $S = 100$. The four regions of supersonic flow visible in Fig. 1(b) have moved clockwise and outward, compressing the fluid ahead of them and forming shocks around $t = 1.5$. Because of the periodic boundaries, identical flows squeeze the fluid from opposite directions, producing broad regions of compression. The local Mach number peaks at around 2.0 and 3.0 for $M = 1.0$, $S = 100$, and $M = 1.5$, $S = 50$, respectively. The shock boundaries expand, eventually intersecting at the central X-point ($t = 2.5$), compressing the weak reconnection current structure residing there (Fig. 3), and producing complex transmitted shock structures ($t > 2.5$). The transmitted shocks propagate toward the boundaries, interacting with the "parent" shocks and weakening through dissipation and expansion.

The emerging shocks strongly influence the spatial variation of the magnetic field. Figure 3 shows the evolution of the electric current density over the interval $t = 2$ to $t = 4$ for $M = 1.0$, $S = 100$. Current sheets (SCS) are coincident with all shocks; the sharpest SCS reside at the two strongest shocks. Unlike the subsonic and incompressible systems, therefore, significant dissipation of magnetic energy occurs at regions other than the vicinities of magnetic X-points. The magnetic energy available to drive reconnection at the X-points is thus lower than for $M \leq 0.6$. At $t = 2$, a wide, weak reconnection current sheet (RCS) is present in the center of the grid, where strong reconnection and sharp RCS were observed much earlier in the subsonic and incompressible simulations. Compression of this central region occurs when the shocks intersect at $t = 2.5$. A sharp RCS appears at that time, indicating that significant reconnection and resistive heating are taking place.

The current density peaks at $t \approx 3$, later than in the subsonic cases, and the central RCS is prominent through $t = 6$. (Note that weak current sheets also appear in the vicinity of the shocks transmitted through the center of the grid.) In the $M = 1.5$ calculation, reconnection is delayed more significantly, reaching a peak at approximately $t = 4$.

The dilatation evolves similarly to the shock current sheets while significant vortex structures reside with both the reconnection current sheet and the shocks. Figure 4 shows the time development of the dilatation. High negative values near the shocks indicate that strong compression is occurring there. The weakening compression with time, evident in the decreasing minimum values, is due to the relatively low Lundquist numbers of the simulations and to the expansion of the shocks that were transmitted through the central reconnection region. Vortex structures occur in regions of greatest shock curvature, and an additional quadrupolar vortex resides at the central RCS, as in the incompressible and subsonic calculations [1]. The quadrupolar vortex structures experience increasing distortion with increasing Mach number. Figure 5 shows that, when the shocks reach the center of the grid at $t = 2.5$, shock vortex structures diagonally bisect the reconnection vortex quadrupoles.

In the incompressible and subsonic systems, the alignment (or correlation) of the velocity and magnetic fields grows over time from the initial value of 50% (cf. I). The onset of this growth occurs slightly later in the subsonic simulations, the delay increasing with M. The next subsection shows that the supersonic cases undergo similar growth of correlation after much larger initial delays. The period of growth ends with a plateau or a period of much slower growth. The correlation value at the plateau is lower as Mach number increases. Retardation of reconnection, as demonstrated by the above contour plots, appears to be a significant factor in reducing the rate of growth and level of correlation between the velocity and magnetic fields relative to the cases for which $M \leq 0.6$. Figures 6(a) and (b) show streamline and magnetic field line plots at $t = 3$ for $M = 1.0$, $S = 50$. The magnetic field has been compressed along the horizontal direction and stretched in the vertical direction relative to the subsonic systems. The shocks themselves cause a kink in the magnetic field, but their presence is much less apparent than in the electric current density, which depends on field gradients. The field lines are bent toward the shock fronts; hence, we are observing "fast" shocks. The velocity field at $t = 3$ shows the early stages of reconnection similar to the situation at $t = 1$ for $M \leq 0.6$. In particular, an X-point forms in the velocity field near the center of the grid, where the X-point in the magnetic field resided at time $t = 0$. This X-point in the velocity field remains in the center of the grid until $t = 6$. By that time, dissipation has significantly reduced both the intensity of reconnection and the effects related to shocks. In Figs. 6(c) and (d), the velocity and magnetic fields at $t = 7$ exhibit mainly a large-scale similarity. We address this more thoroughly in the next subsection through a discussion of the correlation between the momentum and magnetic fields.

The explanation for the delay and suppression of reconnection lies partly in the outward movement of the supersonic regions due to the initial imbalance between the centrifugal force of the magnetofluid and the opposing thermal and magnetic pressures. This rarefies the region near the central magnetic X-point and opposes the flow of fluid into the reconnection region. The time at which shocks reach the center of the grid marks the arrival of appreciable fluid from the outer regions. Only then does one observe rapid reconnection and energy dissipation, as seen at earlier times for $M \leq 0.6$. The presence of current sheets at the shocks also weakens reconnection by rapidly dissipating magnetic energy that would otherwise be dissipated at the magnetic X-point. The transmitted shocks propagating away from the reconnection region, although weak, impede the flow of fluid into that region, somewhat reducing the intensity of reconnection.

In summary, our simulations show that the emergence of shocks outside of a magnetic X-point can impede reconnection at the X-point through Ohmic dissipation of magnetic energy and through rarefaction of the reconnection region itself. Shocks reaching the X-point compress the reconnection region and signal the arrival of higher density magnetofluid, accelerating the reconnection process. We expect the emergence of compressed regions bounded by shocks to affect reconnection similarly in a realistic turbulent MHD flow with local supersonic regions or pressure-momentum imbalances. In a more general situation, reconnection might be enhanced in one region by compression while being delayed by rarefaction or shock-related Ohmic dissipation in a neighboring area.

Figure 7 shows the evolution of the mass density. Note that the system exhibits 180° rotational symmetry, as does the initial magnetic field. Fluid and magnetic field squeezed by the four initial supersonic regions (Figs. 1 and 2(a)) have been pushed rapidly along a direction tangential to the bounding shocks (those which emerged at $t = 1.5$) and inward toward the middle of the system. At $t = 2$, the shocks at the upper left-hand (ULH) and lower right-hand (LRH) regions extend to the central region, and the remaining shock structures appear to include Mach stems. The magnetofluid along that diagonal (ULH shock - central region - LRH shock) is rarefied while the compression regions in the other quadrants consist of two narrow plateaus separated by a narrow region of somewhat lower density. At $t = 2.5$, the ULH and LRH shocks have intersected at the center, compressing the reconnection current sheet and the magnetofluid. The circular patterns at the left and right ends of the RCS correspond to the ends of the fluid jet. In Fig. 7(c) ($t = 3$), the corners of the transmitted shocks and intersections of the primary or incident shocks have introduced additional local density peaks in the region of the jet. By $t = 4$, the density extrema have coalesced and spread and the transmitted shocks have expanded and weakened, interacting with the primary shocks that preceded reconnection. Figure 7(e) shows the mass density at the end of the calculation ($t = 8$). The maximum and minimum values indicate that the mass density is evolving toward a uniform state, consistent with the dissipative nature of the medium. However, because of multiple shock interactions with the density field during the system evolution [20] and because of the injection of small scale fluctuations by magnetic reconnection, the fluid has a turbulent appearance with sizable fluctuations at a range of scales, as mentioned at the beginning of this section.

B. Evolution of Global Properties

B.1. Mach Number Dependence

The $M = 0.6$, $S = 50$, calculation described by Dahlburg and Picone [1] provides a useful baseline for evaluating the evolution of global properties related to dynamic alignment, to production of vorticity and electric currents, and to energy transfer among MHD variables due to reconnection, dynamo action, and shocks. Figure 8 shows the evolution of several global parameters for the simulations with $S = 50$ and $M = 0.6,\ 1.0,$ and 1.5.

Figure 8(a) shows the compressible coefficient of correlation between the momentum and magnetic fields:

$$\alpha_c = \frac{\langle \rho \mathbf{v} \cdot \mathbf{B} \rangle}{\sqrt{\langle (\rho |\mathbf{v}|)^2 \rangle \, \langle |\mathbf{B}|^2 \rangle}} \quad . \tag{13}$$

For the compressible, supersonic, Orszag-Tang vortex system studied here, $\alpha_c = 0.5$ at $t = 0$. As indicated previously [1], the growth of α_c relates to the process of "dynamic alignment" in turbulent, compressible magnetofluids. In incompressible models, dynamic alignment occurs as the kinetic and magnetic energy decay selectively with respect to the cross helicity. The measure often used in incompressible calculations is, therefore, the ratio of the cross helicity (H_c) to incompressible total energy (E_i), given by

$$\xi = \frac{H_c}{E_i} = \frac{2\langle \mathbf{v} \cdot \mathbf{B} \rangle}{\langle |\mathbf{v}|^2 \rangle + \langle |\mathbf{B}|^2 \rangle} \quad . \tag{14}$$

In all of our investigations, the two measures of correlation have qualitatively similar evolutions and provide useful measures of differences among incompressible, subsonic, and supersonic MHD flows.

Figure 8(a) shows that the baseline subsonic system ($M = 0.6$) undergoes more rapid growth in α_c than do the supersonic cases ($M \geq 1$)). In fact, the $M = 0.6$ calculation has two stages of rapid growth (for $t \leq 8$), beginning at approximately $t = 1.5$ and 4.5, respectively, and ending with plateaus at successively higher correlation values. The correlation

α_c in each of the supersonic calculations exhibits only a single stage of rapid growth to a plateau for $t \leq 8$, beginning at $t \approx 3.5$ when $M = 1.0$ and at $t \approx 4.5$ when $M = 1.5$. The supersonic systems also experience an early stage in which the correlation level wanders around the initial value of 0.5 before the onset of rapid growth. The end of this initial "induction period" occurs at roughly the same time as the peak in the current density in the reconnection region (Section III.A.). Incidentally, the $M = 0.6$ curve shows an initial period of slow growth which also ends when the current density peaks in the reconnection region, in this instance at $t \approx 2.0$. Figure 8(a) shows that the plateau value of α_c at late times varies approximately linearly with the reciprocal of the characteristic Mach number M.

In the compressible Orszag-Tang vortex model, growth of correlation thus appears to depend strongly upon the dynamics of, and energy dissipation by, reconnection at the central magnetic X-point. As indicated in the previous subsection, the supersonic flows in the Orszag-Tang vortex initially rarefy the plasma in the central region, weakening reconnection there. Shocks bound the regions of high density, so that the arrival of shocks in the reconnection region is a precursor to considerable inflow of magnetofluid. The latter inflow is, in turn, necessary for significant reconnection to occur, and α_c begins sustained growth shortly thereafter. The increased delay in sustained growth of correlation with increasing Mach number thus corresponds to the later arrival of the shocks at the central X-point. In addition, as the characteristic Mach number increases, the shocks become stronger, as do the current sheets associated with them. Then the amount of magnetic and kinetic energy transformed into internal energy at the shocks also must increase with M. This leaves less energy to drive reconnection and, consequently, dynamic alignment, causing the value of α_c at a given time to be lower as the Mach number increases. Following the rapid growth of correlation, all cases reach a stage of very slow growth, after the reconnection event has run its course.

Figures 8(b) and (c) show the temporal evolution of the kinetic energy (normalized to one) and magnetic energy for various Mach numbers. The dependence of both on $M \geq 1$

is much stronger than for the subsonic flows ($M \leq 0.6$), which showed little variation with Mach number. In incompressible numerical simulations [10], the oscillations in kinetic and magnetic energy were approximately 180° out of phase and were interpreted as Alfvénic. Our subsonic calculations [1] were quite similar to the incompressible calculations in this regard, and the same interpretation applied, since the initial kinetic and magnetic energies were equal and smaller than the internal energy by a factor of at least five and because the effects of acoustic waves were small. In the present calculations, however, the initial kinetic energy increases as M^2 while the initial magnetic energy remains at unity. In addition, shocks and magnetoacoustic waves are present, so that the temporal evolutions of the magnetic and kinetic energies are not linked in the same manner as for the subsonic and incompressible systems. The increased magnitude of the kinetic energy as M increases explains the greater relative sensitivity of the magnetic energy to supersonic Mach number (Fig. 8(c) vs. 8(b)). Small percentage changes in kinetic energy could result in larger relative changes in the magnetic energy, whereas small fluctuations in the magnetic energy would affect the kinetic energy even less.

Additional phenomena should affect the evolution of the magnetic energy shown in Fig. 8(c). First, appreciable reconnection is delayed and apparently weakened as the Mach number increases. Second, given that we are observing fast shocks, compression should enhance the magnetic energy, leading to larger peak values with increasing Mach number. Because of the larger jump in tangential magnetic field across the shock with higher Mach number, the dissipation of magnetic energy by the shocks and their associated shock current sheets also should increase with Mach number. In Fig. 8(c), the peak magnetic energy and the subsequent dip are both proportionately larger for $M = 1.5$ than for $M = 1.0$. In addition, the final stage of decreasing magnetic energy occurs later because the stage of strong reconnection is delayed. Notice that a shoulder appears at $t \approx 3.5$ for $M = 1.0$ and at $t \approx 4.5$ for $M = 1.5$. These are the respective times at which the rapid growth of correlation began.

In I, our interpretation of the temporal evolution of the $M = 0.6$ calculation was different from that in the previous paragraph because no shocks were present. In Fig. 8(c), the magnetic energy is enhanced at $t \approx 2$ when $M = 0.6$. This is later than for the supersonic cases and is consistent with an Alfvénic exchange of energy from the momentum field to the magnetic field, similar to that occurring in incompressible media [1, 21]. The subsequent decay of magnetic energy is more immediate than in the supersonic calculations, and no "shoulder" appears in the curve. We attribute this to the fact that strong reconnection is not delayed when M is subsonic [1]. An Alfvénic transfer of energy between the momentum and magnetic fields is likely to occur in the supersonic systems as well, and we cannot state with certainty that compressional effects are more important. However, the stronger Mach number dependence of the supersonic cases leads us to believe that the interpretations in the previous paragraph are reasonable.

Figures 8(d) shows the evolution of the kinetic enstrophy, $\langle \omega^2 \rangle$, where ω is the vorticity. The decrease and delay in kinetic enstrophy production relative to the subsonic calculation ($M = 0.6$) must relate to shock formation and the delay in appreciable reconnection, as discussed previously. Here the initial rise in enstrophy occurs when shocks first emerge, indicating that shock curvature is contributing significantly to vorticity production, according to Crocco's Theorem [22]. The structure in the supersonic systems depends in a complicated manner upon shock formation and interactions, as well as upon vorticity production at the central reconnection current sheet and the secondary RCS residing on the boundaries.

Figure 8(e) shows the magnetic enstrophy, $\langle j^2 \rangle$, where j is the electric current density. The effects of shock emergence on magnetic energy dissipation appear prominently in the form of a massive enhancement at $t \approx 1.5$ for $M = 1.5$ and as a smaller peak for $M = 1.0$. The supersonic cases have similarly sized peaks at $t \approx 3$ ($M = 1.0$) and $t \approx 4$ ($M = 1.5$), corresponding to reconnection at the central magnetic X-point. In contrast, the broad enhancement in the subsonic system indicates that steady reconnection occurs at approximately the same level over the interval $1.0 \leq t \leq 3.0$. The final stage of decay occurs later as the Mach number increases.

B.2. Lundquist Number Dependence

Figure 9 shows global averages corresponding to $M = 1.0$ and $S = 50$, 100, and 200 for $0 \leq t \leq 8.0$. In Fig. 9(a), the compressible correlation coefficient, α_c, shows the same qualitative behavior as in the analogous subsonic and incompressible simulations [1], with the degree of alignment at a given time decreasing as S increases. The kinetic energy (Fig. 9(b)) also displays similar behavior to its subsonic counterparts, with almost no Lundquist number dependence during the early stage of development. However, the timing of the fluctuations in average kinetic energy is different from that of the subsonic calculations (Fig. 5(c), I). The fact that the initial kinetic energy in Fig. 9 is nearly three times the initial magnetic energy means that the latter affects the kinetic energy much less than in the subsonic flows. Apparently the compression of the fluid downstream of the initial high Mach number regions and the formation of shocks reduce the kinetic energy and transfer energy to the magnetic field. This energy transfer occurs through Alfvén waves in an incompressible magnetofluid.

The evolution of magnetic energy as a function of Lundquist number (Fig. 9(c)) is less similar to that in the subsonic cases. The initial extremum in magnetic energy occurs earlier, at $t \approx 1.5$, when shocks form, as opposed to $t \approx 2$ for $M \leq 0.6$. For $S = 100$ and 200, a second extremum appears at $t \approx 4$ which is not seen for $S = 50$ or for $M \leq 0.6$. This is most likely due to a combination of two factors:

(1) Following the arrival of the "incident" shocks at the central magnetic X-point and the onset of strong reconnection there, transmitted and diffracted fast shock waves interact with the reconnection current sheet and with remnants of the incident waves. The array of shocks no longer forms a network bounding quasistationary regions, as seen at earlier times. Instead the shocks expand and propagate through a large portion of the system, compressing the magnetic field and increasing the magnetic energy. Interactions among the

various shocks and magnetoacoustic waves enhance the complexity of the wave structure over time. The coverage of the grid by these waves thus increases with time for $t > 1.5$, and their influence later diminishes as dissipative effects become more prominent for $t > 4.0$. This sequence is implicit in the broad peak observed in Fig. 9(b).

(2) The reduced rate of dissipation of shock waves and other magnetoacoustic waves at higher Lundquist numbers increases the strength of the compression. The broad peak in magnetic energy at $t \approx 4$ thus becomes more prominent as Lundquist number increases.

Figures 9(d) and (e) show that the kinetic and magnetic enstrophies increase approximately linearly with Lundquist number and have similar structures. Distinct peaks emerge at $t \approx 3$ and $t \approx 4$ as dissipation decreases. The peak at $t = 3$ corresponds to the time at which the current in the reconnection region reaches a maximum. As in Fig. 9(c), the peak in current density at $t = 4$ reflects the wide distribution and interactions of numerous magnetoacoustic waves and shock waves, following the arrival of the "incident" shock waves at the central magnetic X-point. The subsequent onset of strong reconnection and the transmission and diffraction of the incident shocks through the reconnection region (e.g., Fig. 2(d)) results in a complex global magnetic-field structure with significant gradients throughout the system at $t \approx 4$. Figure 3(d) verifies this, showing the presence of sizable currents over a large portion of the grid at that time.

C. Spectral Decompositions of Correlations

Here we examine the calculation with $M = 1.0$, $S = 100$, although the trends identified are consistent across all of the simulations under discussion. Prior to the formation of shocks at $t \approx 1.5$, the wavenumber spectra are typical of decay problems and resemble those of the subsonic cases [1]. Figure 10(a), for example, shows the mass density autocorrelation spectrum at $t = 1$. However, after shocks form, the wavenumber spectra of the mass density, velocity, nonsolenoidal and solenoidal components of the velocity, and the magnetic field appear quite changed, as shown in Fig. 10(b) and (d) - (g) for time $t = 2.0$. Except at wavenumber extremes, each is approximately linear, with a slope similar to that of the reference line (k^{-4}). The magnetic field deviates from the others, showing a slightly steeper slope. The magnetic field spectrum also differed from that of the other functions in the subsonic simulations.

This change of spectrum coincides with the emergence of compressed regions bounded by shocks. With the passage of time, the high wavenumber portion of the spectrum falls from the reference line as a result of dissipation. The density spectrum in Fig. 10(c) exemplifies that effect. In an effort to model the spectral features of these compressed regions, J. Dahlburg [23] has computed numerically the equivalent spectra of elevated plateaus with either square or circular cross sections. The circular enhancement produced an approximate k^{-3} autocorrelation spectrum. The square plateau had two distinct components: k^{-2}, characteristic of a one-dimensional planar shock, and approximately $k^{-3.5}$. Since the actual structures have cross sections similar in a very coarse view to a quadrilateral, the square "model" is closer to the simulations. These considerations show that simple idealizations of the two-dimensional compressed regions are not entirely adequate to explain our observations quantitatively. However, the qualitative results do seem to explain the change in autocorrelation spectra which we observe when two-dimensional compressed regions with bounding shocks appear.

Figure 11(a) and (b) show the spectral amplitude of the cross-helicity normalized by the spectral amplitude of the incompressible energy at $t = 2.0$ and 6.0, respectively. In the subsonic cases, the low wavenumber region had positive values while the high wavenumber region showed an anticorrelation, although this bifurcation was less pronounced at $M = 0.6$ than at $M = 0.2$. Here we see that the velocity and magnetic field are approximately uncorrelated over most of the spectrum at times prior to the interaction of the shocks near the X-point. For later times ($t \geq 4$) with $M = 1.0$, the lower and middle wavenumbers show a positive correlation while the higher wavenumber components are approximately uncorrelated. For $M = 1.5$, $S = 50$, the middle and higher wavenumber portions of the spectrum are uncorrelated, while the lower wavenumbers have positive values throughout the calculation. The presence of two-dimensional compressed structures bounded by shocks, the coincident dissipation of energy by the shock current sheets, and the delay and reduction of energy dissipation by reconnection are the likely causes of the reduction of correlation at the smaller scales. In addition, these factors probably are responsible for the lower global (average) correlation between the magnetic and velocity fields relative to subsonic flows.

Mechanisms which suppress the growth of correlation between the velocity and magnetic fields at temporal scales of a few hours or less are of interest in interpreting measurements of the solar wind [24]. The above compressive mechanism can occur at the scale of any nonuniformity within, or encountered by, the solar wind. This is because such nonuniformities can generate shocks, given that the solar wind is supersonic and is not a steady flow. Presently the excitation of Kelvin-Helmholtz instability by velocity shear is the leading candidate for the cause of a reduction in correlation between the magnetic and velocity fields with increasing distance from the Sun [24]. We point out that the interpretation of the data is still uncertain. For example, early data analysis indicated that MHD fluctuations in the solar wind are mainly Alfvénic and propagate away from the Sun [25]. Subsequent theoretical work inferred from this observation that the population of either the aligned or the antialigned state would become dominant with increasing distance from the Sun (e.g., [26]). Recent data analysis has indicated a much smaller population of outwardly propagating Alfvénic fluctuations near the earth. This has led to the conclusion that neither state of alignment dominates at distances around 1 AU from the Sun.

The correlation of the fluctuations in thermal and magnetic pressures is mostly negative soon after the shocks have formed, as exemplified by Fig. 11(c). At later times ($t > 3.0$), this effect becomes less pronounced or disappears entirely, depending on M and S. According to arguments by Barnes [27], a negative correlation is consistent with the presence of quasistationary structures in the flow field. Clearly such structures exist here until the bounding shocks reach the central magnetic X-point, after which time the shocks weaken and the original compressed regions change significantly. This could explain the above observation that the negative correlation disappears at later times. In their studies of weakly compressible turbulence, Shebalin and Montgomery [6] have found that gradients of the total pressure (thermal plus magnetic) relax away at the higher wavenumbers. Their studies differ from the present ones in that we are concerned with supersonic flows, for which the fluctuations in thermal pressure and mass density are not necessarily proportional.

In the present calculations, the mass density and magnetic pressure showed no long-lived or readily discernable trends in spectral correlation, unlike the thermal pressure and the magnetic field. We can understand this through the following:

(1) In MHD flows, the mass density changes in response to total pressure, which includes contributions from both magnetic and thermal pressures, and

(2) In compressible flows, the mass density and thermal pressure fluctuations need not be highly correlated due to the influence of entropy fluctuations.

The mass density and magnetic pressure did, however, show a net positive (spatially averaged) correlation during the evolution of the system at average Mach number $M = 1.5$. At such high Mach numbers, compression of the magnetic field and the fluid at the shocks most likely dominates the average correlation (over the grid) and could be sufficient to give a net positive correlation.

IV. Summary

The Orszag-Tang vortex system provides a spatially periodic model of a magnetofluid undergoing transition to turbulence. The model demonstrates the emergence of small scale structure through magnetic reconnection and current sheet formation. Over time, dynamic alignment of the momentum and magnetic fields occurs. The Orszag-Tang system also represents an easily reproducible set of initial conditions for comparisons among different numerical models of MHD. The present calculations and those described in I extend the set of numerical results to compressible MHD flows, including those which are moderately supersonic. We have found that the presence of embedded supersonic flows and the existence of local force imbalances at moderately high β can cause fast shocks and broad compressions. The evolution and structure of the "supersonic" Orszag-Tang system, therefore, differ significantly from those of its subsonic and incompressible counterparts. The same phenomena will occur in any turbulent magnetofluid with embedded supersonic regions and local properties similar to the Orszag-Tang system. As a consequence, we predict that many structural, global, and spectral properties of such a medium will differ substantially from those of subsonic and incompressible turbulent MHD flows. Here we summarize those properties.

In the Orszag-Tang vortex system, the presence of moderately supersonic regions ($\mathcal{M} \approx 2$) can result in the emergence of shocks in the region outside of the magnetic X-point. Accompanying the shocks are prominent current sheets, which dissipate magnetic energy. Such current sheets were not present in our subsonic and incompressible calculations. In addition, vortex structures reside in regions of changing shock curvature. The shocks occur when the forces due to thermal and magnetic pressure do not balance the distribution of momentum in the initial conditions. The excess centrifugal force pulls fluid away from the central X-point, rarefying the region and delaying significant reconnection there. Since the shock current sheets dissipate magnetic energy at early times, the reconnection is weaker as the initial supersonic Mach number increases. The intensity of the reconnection increases significantly when the shocks (and the dense fluid which they bound) reach the region of the original X-point. The correlation of the momentum and magnetic field begins growing rapidly thereafter. Eventually the growth slows considerably so that the correlation reaches a "plateau," which decreases with increasing Mach number. The present model does not indicate with certainty whether reconnection always is enhanced and accelerated by compressive fluid motions and inhibited by rarefying motions. However, both effects occur in the present calculations.

The compressed regions bounded by shocks dominate autocorrelation spectra at early times, including that of the solenoidal velocity component. We have not yet explained why the latter occurs, other than to infer that the solenoidal and nonsolenoidal components are closely coupled and to note that solenoidality of the flow does not imply incompressibility of the medium. As opposed to the subsonic and incompressible cases, the normalized spectral correlation between the velocity and magnetic fields is near zero over the middle and upper portions of the wavenumber domain. The correlation between thermal and magnetic pressure is negative over a wide wavenumber range at early times for all calculations with $M \geq 1.0$. This is consistent with the presence of broad, long-lived regions of compression. At later times, these regions are disrupted and the spectral anticorrelation of thermal and magnetic pressures disappears.

To complete our investigation of the compressible Orszag-Tang model, we are currently investigating the effect of varying β on the above conclusions. The present and previous simulations set $\beta \geq 10/3$, so that the magnetic field has not played as dominant a role as it might in some space or laboratory plasmas. Our next step in the study of compressible MHD turbulence will be to investigate the decay of magnetofluids from random initial conditions with and without embedded supersonic flows.

V. Acknowledgements

The authors wish to thank the National Aeronautics and Space Administration (NASA: Solar-Terrestrial Theory Program and its successor, the Space Physics Theory

Program) and the Office of Naval Research for generous support of this work. We performed the calculations on the NASA Ames Research Center Cray Y-MP under the Numerical Aerodynamic Simulation Program. The authors are grateful to J. Dahlburg for calculations and assistance in analyzing correlation spectra. We thank J. Dahlburg, J. T. Karpen, and J. H. Gardner for reviewing the paper carefully, for suggesting improvements in the presentation, and for clarifying important physical processes. We are also grateful for helpful discussions with J. P. Boris, S. K. Antiochos, J. T. Mariska, and S. G. Lambrakos.

References

1. R. B. Dahlburg and J. M. Picone, *Phys. Fluids B* **1**(11), 2153 (1989).
2. J. M. Picone and J. P. Boris, in *Proceedings of the Eighth International Conference on Numerical Methods in Fluid Dynamics*, ed. by E. Krause (Springer-Verlag, New York, 1982), pp.408-13.
3. J. R. Greig, R. E. Pechacek, and M. Raleigh, *Phys. Fluids* **28**(8), 2357 (1985).
4. S. Klainerman and A. Majda, *Comm. Pure Appl. Math.* **34**, 481 (1981).
5. D. Montgomery, M. R. Brown, and W. H. Matthaeus, *J. Geophys. Res.* **92**(A1), 282 (1987).
6. J. V. Shebalin and D. Montgomery, *J. Plasma Phys.* **39**(2), 339 (1988).
7. W. H. Matthaeus and M. R. Brown, *Phys. Fluids* **31**(12), 3634 (1988).
8. S. A. Orszag and C.-M. Tang, *J. Fluid Mech.* **90**, 129 (1979).
9. R. B. Dahlburg, J. M. Picone, and J. T. Karpen, *J. Geophys. Res.* **93**, 2527 (1988).
10. A. Pouquet, P.-L. Sulem, and M. Meneguzzi, *Phys. Fluids* **31**, 2635 (1988)
11. H. Politano, A. Pouquet, and P. L. Sulem, *Phys. Fluids B* **1**(12), 2330 (1989).
12. R. Peyret and T. D. Taylor, *Computational Methods for Fluid Flow* (Springer-Verlag, New York, 1983).
13. R. B. Dahlburg, T. A. Zang, D. Montgomery, and M. Y. Hussaini, *Proc. Nat. Acad. Sci. USA* **80**, 5798 (1983).
14. G. Erlebacher, M. Y. Hussaini, C. G. Speziale, and T. A. Zang, in *Numerical Methods in Laminar and Turbulent Flow*, edited by C. Taylor, W. G. Habashi, and M. M. Hafez (Pineridge, Swansea, UK, 1988), p. 1932.
15. R. B. Dahlburg and J. M. Picone, *Comp. Meth. Appl. Mech. Eng.* (1990), in press.

16. W. S. Dorn and D. D. McCracken, *Numerical Methods with FORTRAN IV Case Studies* (John Wiley & Sons, New York, 1972), 369.

17. T. Passot and A. Pouquet, *J. Fluid Mech.* **181**, 441 (1987).

18. J. M. Picone and J. P. Boris, *Phys. Fluids* **26**(2), 365 (1983).

19. J. M. Picone and J. P. Boris, *J. Fluid Mech.* **189**, 23 (1988).

20. J. M. Picone, E. S. Oran, J. P. Boris, and T. R. Young, in *Dynamics of Shock Waves, Explosions, and Detonations (Progress in Astronautics and Aeronautics, Vol 94)*, ed. by J. R. Bowen, N. Manson, A. K. Oppenheim, and R. I. Soloukhin (AIAA, New York, 1985), 429.

21. P.-L. Sulem, A. Pouquet, and M. Meneguzzi, in *Advances in Turbulence*, ed. by G. Compte-Bellot and J. Mathieu (Springer, New York, 1987), p.291.

22. A. H. Shapiro, *The Dynamics and Thermodynamics of Compressible Fluid Flow, Vol. 1* (Wiley, New York, 1953), pp. 281-2.

23. J. Dahlburg, private communication (1989).

24. D. A. Roberts, L. W. Klein, M. L. Goldstein, and W. H. Matthaeus, *J. Geophys. Res.* **92** A10, 11021 (1987).

25. J. W. Belcher and L. Davis, *J. Geophys. Res.* **76**(16), 3534 (1971).

26. M. Dobrowolny, A. Mangeney, and P. Veltri, *Phys. Rev. Lett.* **45**(2), 144 (1980).

27. A. Barnes, in *Solar System Plasma Physics, Volume 1*, ed. by E. N. Parker, C. F. Kennel, and L. J. Lanzerotti (North-Holland, New York, 1979), pp.249-319.

APPENDIX A

Pressure Imbalance in the Supersonic Orszag-Tang Vortex System

The present model of supersonic regions within the Orszag-Tang vortex system uses a fluctuating pressure $p_1 \equiv \delta p^0$ which is consistent with Eqs.(6) for an incompressible magnetofluid of initial mass density $\rho^0 = 1$. The corresponding velocity and magnetic fields, denoted by $\mathbf{v}_1$ and $\mathbf{B}_1$, respectively, then satisfy the elliptic equation:

$$\nabla \cdot (\mathbf{v}_1 \cdot \nabla \mathbf{v}_1) = \frac{1}{\rho^0}\left[-\frac{1}{2}\, \nabla^2 (p_1 + |\mathbf{B}_1|^2) + \nabla \cdot (\mathbf{B}_1 \cdot \nabla \mathbf{B}_1)\right] \quad . \tag{A.1}$$

Equation (A.1) represents the force balance between the motions of the magnetofluid and the confining thermal and magnetic pressures. The flat background pressure, p^0, and the characteristic Mach number, M, must be consistent with ρ^0 and $|\mathbf{v}^0| \equiv \sqrt{\langle \mathbf{v}_1^2 \rangle}$, through the equation

$$M^2 = \frac{2\rho^0 |\mathbf{v}^0|^2}{\gamma\, p^0} \quad . \tag{9b}$$

For the subsonic cases with $\rho^0 = 1$, Eqs.(A.1), (6), and (9b) represent a consistent specification of the initial conditions. As stated in Section II.B, the constraint on the average pressure p^0 limits its minimum value to $\max\{-p_1(x,y)\} + \epsilon$, where $\epsilon > 0$, so that the local Mach number will be defined everywhere. For $\gamma = 5/3$, Fig. 1 of Dahlburg and Picone [1] shows that p^0 is > 2.6. Equation (9b) then limits the characteristic Mach number to $M \leq 0.679$. Even when p^0 is sufficiently close to 2.6 for supersonic regions to exist within the initial flow field, we do not observe shocks, and the quantitative behavior of such systems is quite close to that of the $M = 0.6$ case presented in **I**.

Equation (9b) shows that one could increase the characteristic Mach number, M, by increasing the amplitude of the initial velocity field, increasing the initial mass density or lowering p^0. If the initial velocity in Eq.(6) were increased by a constant factor, we would also increase the magnetic field amplitude by the same factor in order to maintain the initial normalized cross helicity in Eq.(14) at 0.5. Given this constraint, consider each alternative separately:

(1) Scale the velocity field up by a constant factor. Set $\mathbf{B}' = \alpha \mathbf{B}_1$ and $\mathbf{v}' = \alpha \mathbf{v}_1$ with $\alpha > 1$. Then by Eq.(A.1), $\rho' = 1$, and $p' = \alpha^2 p_1 \Rightarrow p^{0'} > 2.6\alpha^2$. By Eq.(9b), we have $M \leq 0.679$.

(2) Scale the mass density up by a constant factor, so that $\rho' = \alpha$ with $\alpha > 1$. Then by Eq.(A.1), a solution is $\mathbf{v}' = \mathbf{v}_1/\sqrt{\alpha}$, $\mathbf{B}' = \mathbf{B}_1$, and $p' = p_1 \Rightarrow p^{0'} > 2.6$. By Eq.(9b), we have $M \leq 0.679$. Note that this solution also fails to maintain the initial normalized cross helicity in Eq.(14) at 0.5.

(3) Scale the initial pressure down by a constant factor, so that $p' = \alpha p_1$ and $p^{0'} > 2.6\alpha$, where $\alpha < 1$. Equation (A.1) gives the solution $\mathbf{v}' = \sqrt{\alpha}\mathbf{v}_1$, $\mathbf{B}' = \sqrt{\alpha}\mathbf{B}_1$, and $\rho' = 1$. Again Eq.(9b) shows that $M \leq 0.679$.

This shows that one cannot increase M to supersonic values while maintaining the above constraints on $\mathbf{v}$ and $\mathbf{B}$ *and* satisfying Eq.(A.1). We can achieve supersonic values of M only by violating the balance of forces and pressures implied by Eq.(A.1). Hence, our approach is to increase ρ^0 above 2.78 and, at the same time, to allow δp^0, $\mathbf{v}$, and $\mathbf{B}$ to satisfy Eq.(A.1) *with ρ^0 set equal to one.* Since the fluctuating pressure will not balance the other local forces, finite magnetoacoustic waves or shock waves will emerge in the flow.

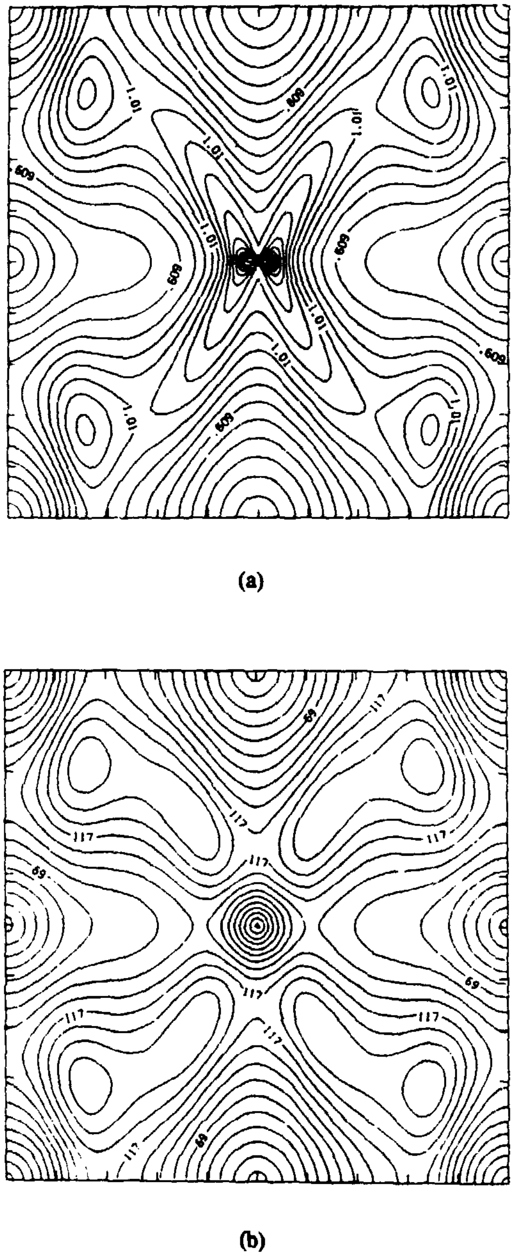

Fig. 1 — Contours of constant local Mach number $\mathcal{M}$ at time $t = 0$. (a) Characteristic Mach number M = 0.679 with balanced forces throughout grid. Minimum value of the initial pressure is 1×10^{-4}. Minimum and maximum values of $\mathcal{M}$ are 0.0 and 2.185. (b) Characteristic Mach number M = 1.0 with unbalanced forces in the grid. Minimum and maximum values of $\mathcal{M}$ are 0.0 and 1.620.

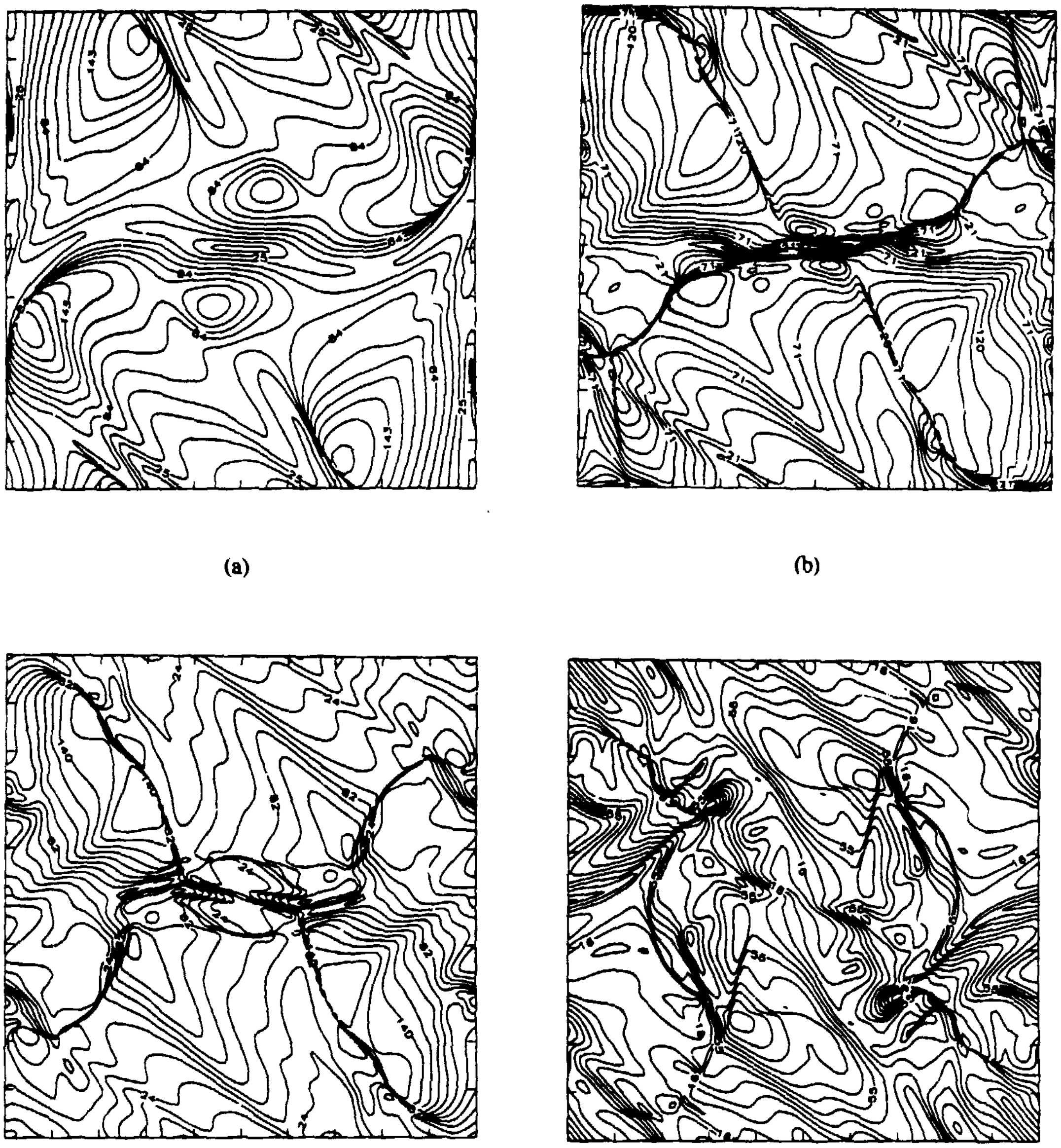

(a) (b)

(c) (d)

Fig. 2 — Evolution of the local Mach number for M = 1.0 and S = 100 (minimum, maximum values): (a) t = 1.5 (0.0, 1.970), (b) t = 2.5 (0.0, 1.659), (c) t = 3.0 (0.0, 1.932), (d) t = 4.0 (0.0, 1.283).

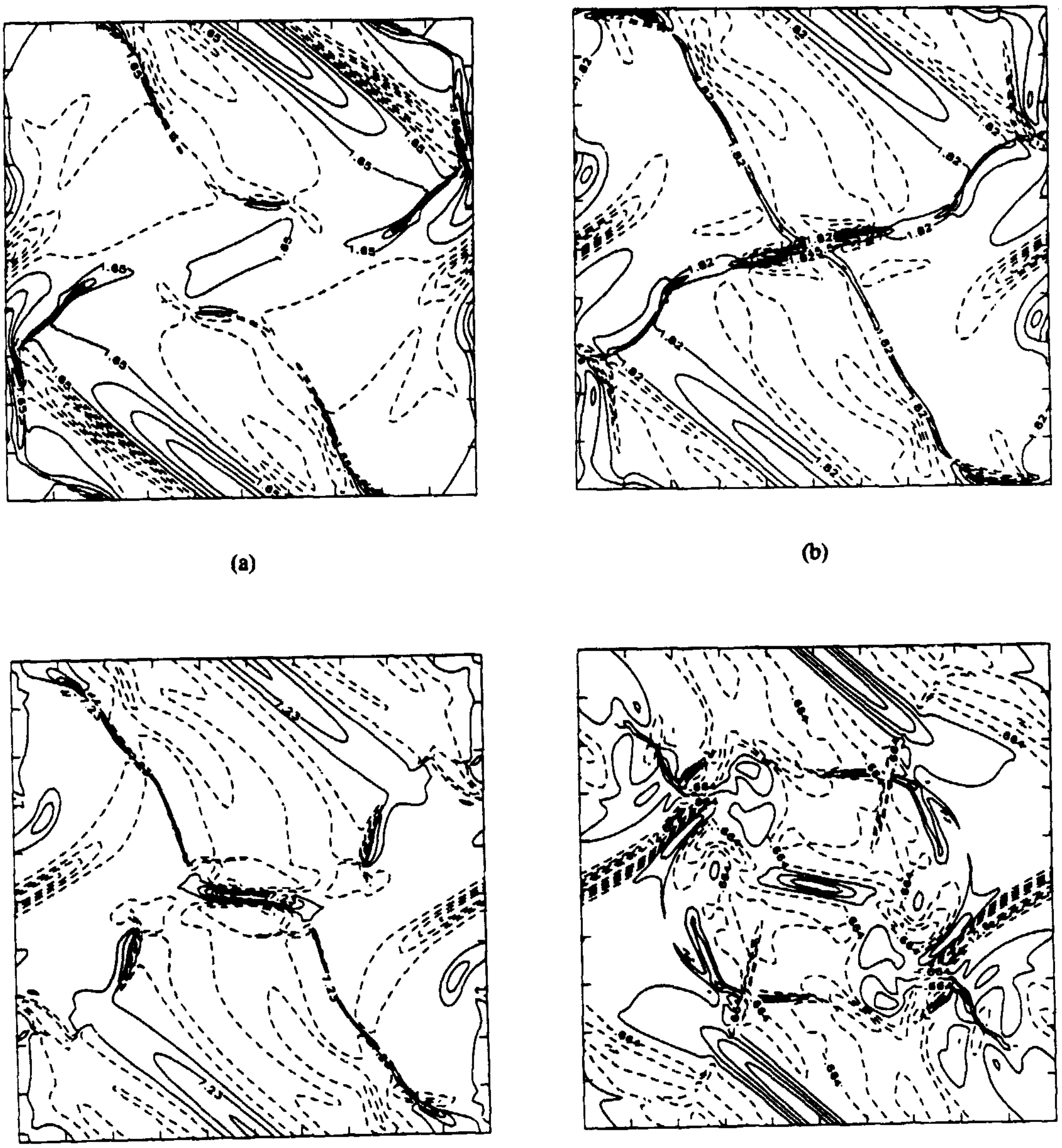

(a) (b)

(c) (d)

Fig. 3 — Evolution of the electric current density for M = 1.0 and S = 100 (minimum, maximum values): (a) t = 2.0 13.1, 21.6), (b) t = 2.5 (-17.6, 28.0), (c) t = 3.0 (-15.6, 38.1), (d) t = 4.0 (-17.6, 22.3).

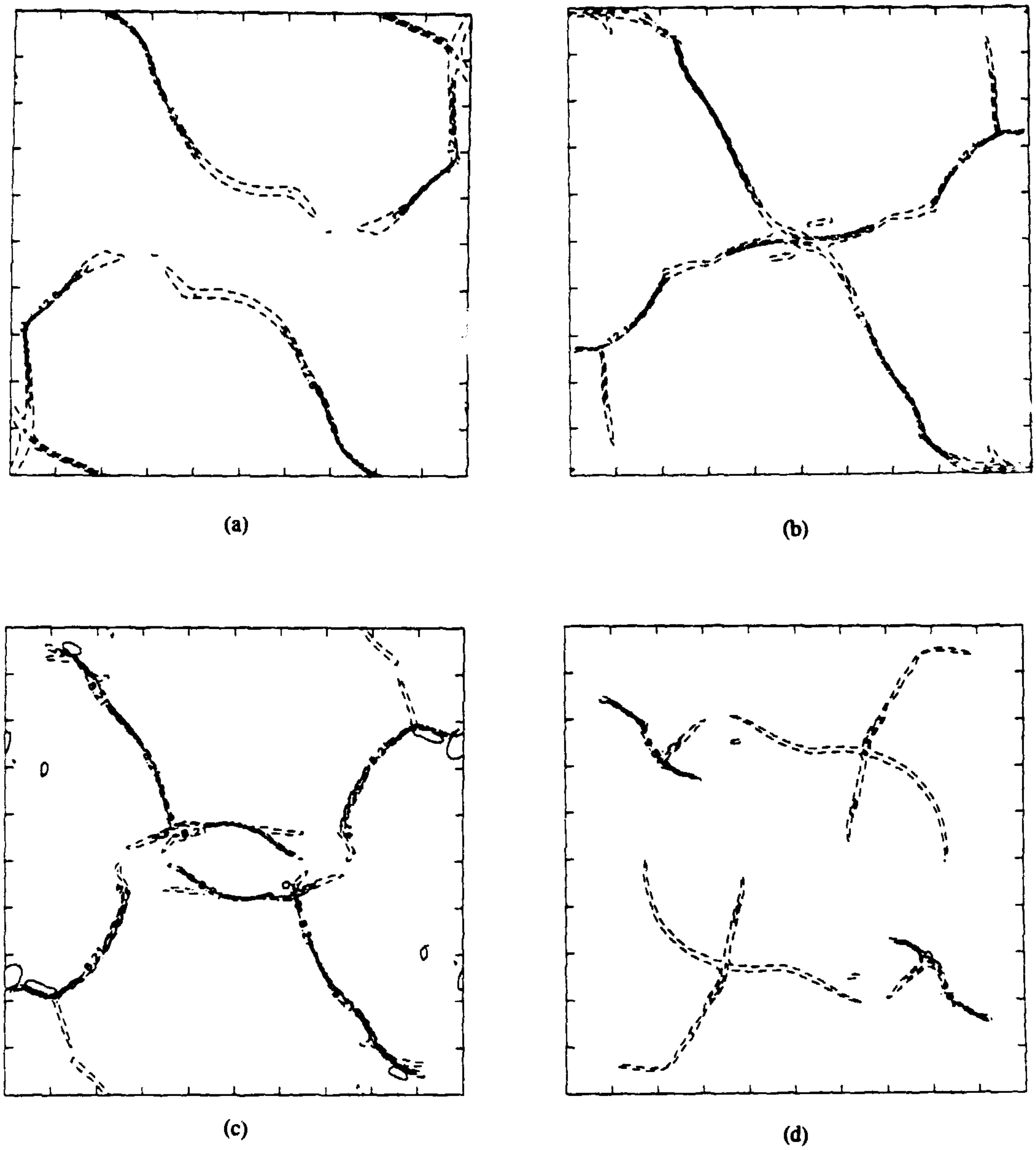

(a)

(b)

(c)

(d)

Fig. 4 — Evolution of the dilatation for M = 1.0 and S = 100 (minimum, maximum values): (a) t = 2.0 (-65.2, 7.4), (b) t = 2.5 (-58.2, 5.4), (c) t = 3.0 (-38.1, 3.1), (d) t = 4.0 (-45.4, 3.6).

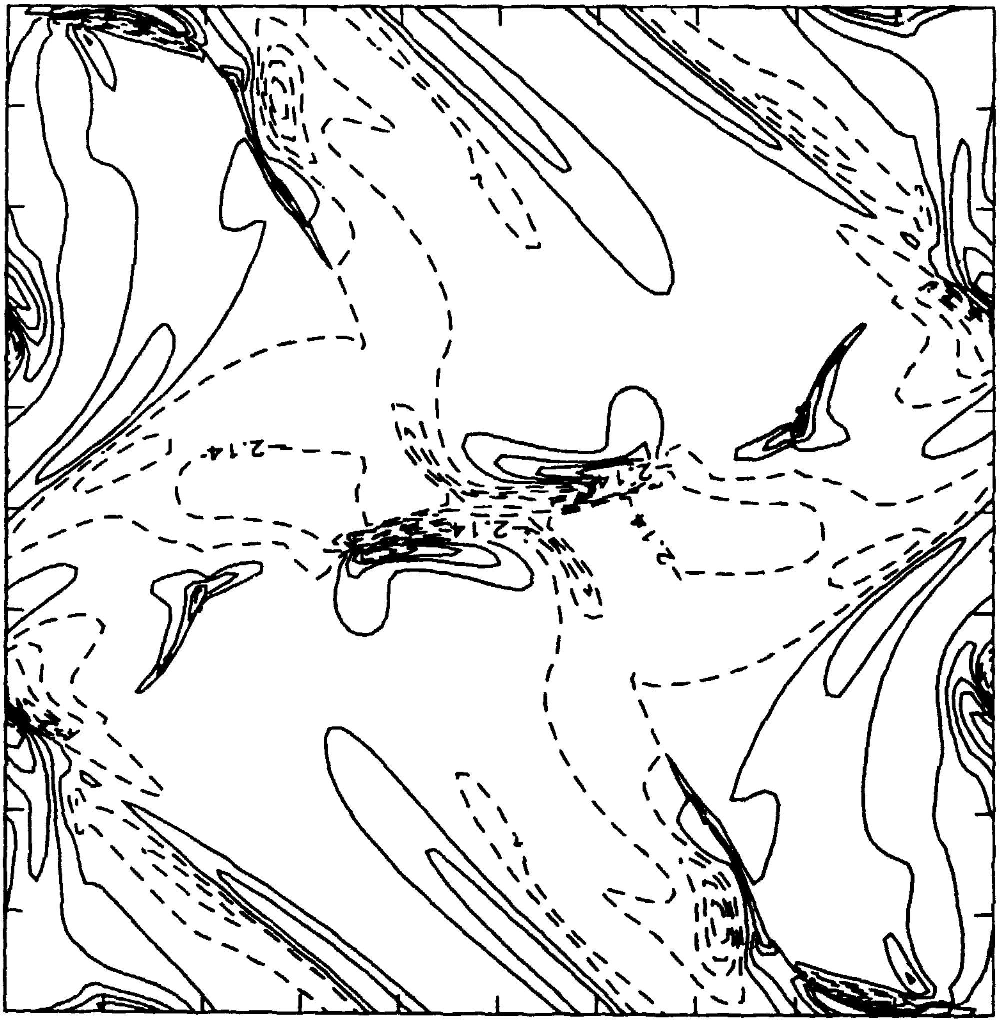

Fig. 5 — Vorticity contours for M = 1.0 and S = 100 at t = 2.5. Minimum value is -9.7 and maximum is 8.0.

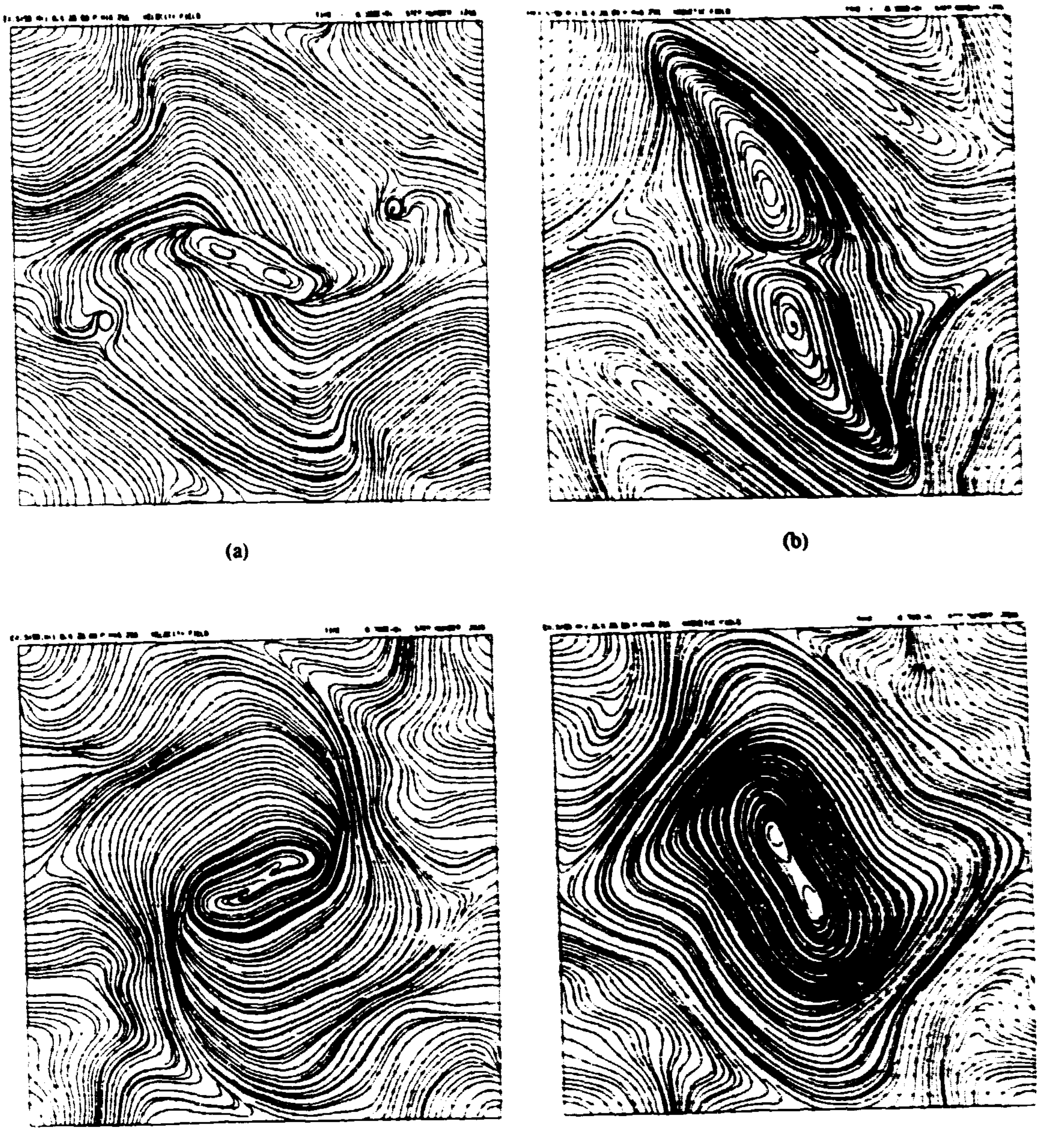

(a)

(b)

(c)

(d)

Fig. 6 — Plots of the generalized stream function for $M = 1.0$ and $S = 50$ giving direction of velocity ((a) and (c)) and magnetic field ((b) and (d)) at respective times $t = 3.0$ and 7.0.

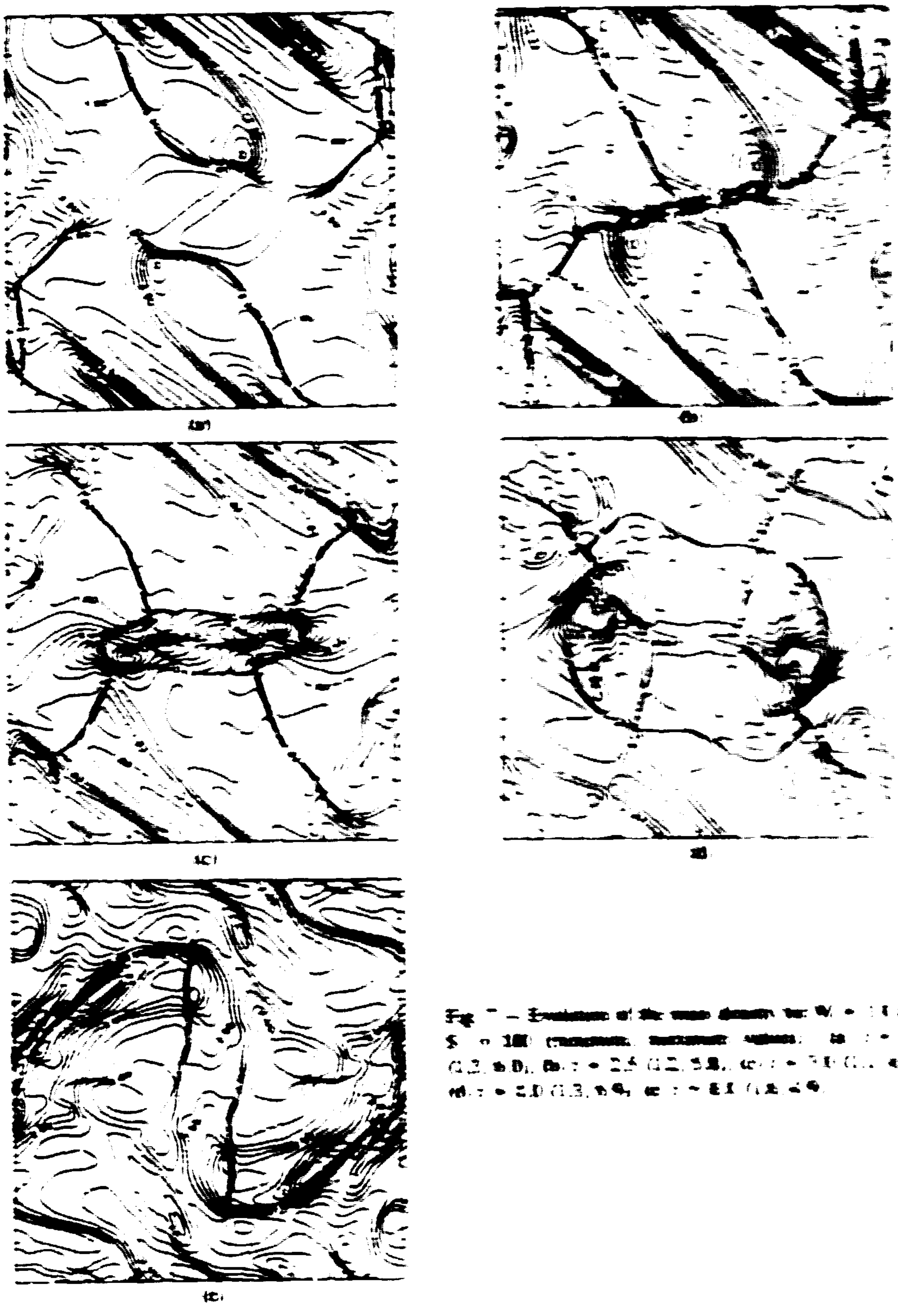

(a)

(b)

(c)

(d)

(e)

Fig. 7 — Evolution of the mass density for [illegible] = [illegible] and S = 100 ([illegible], [illegible] values): (a) t = 2.4 (1.2, 0.0), (b) t = 2.6 (1.2, 0.8), (c) t = [illegible] (1.[illegible], 0.5), (d) t = 2.0 (1.3, 0.6), (e) t = 8.1 (1.8, 0.6).

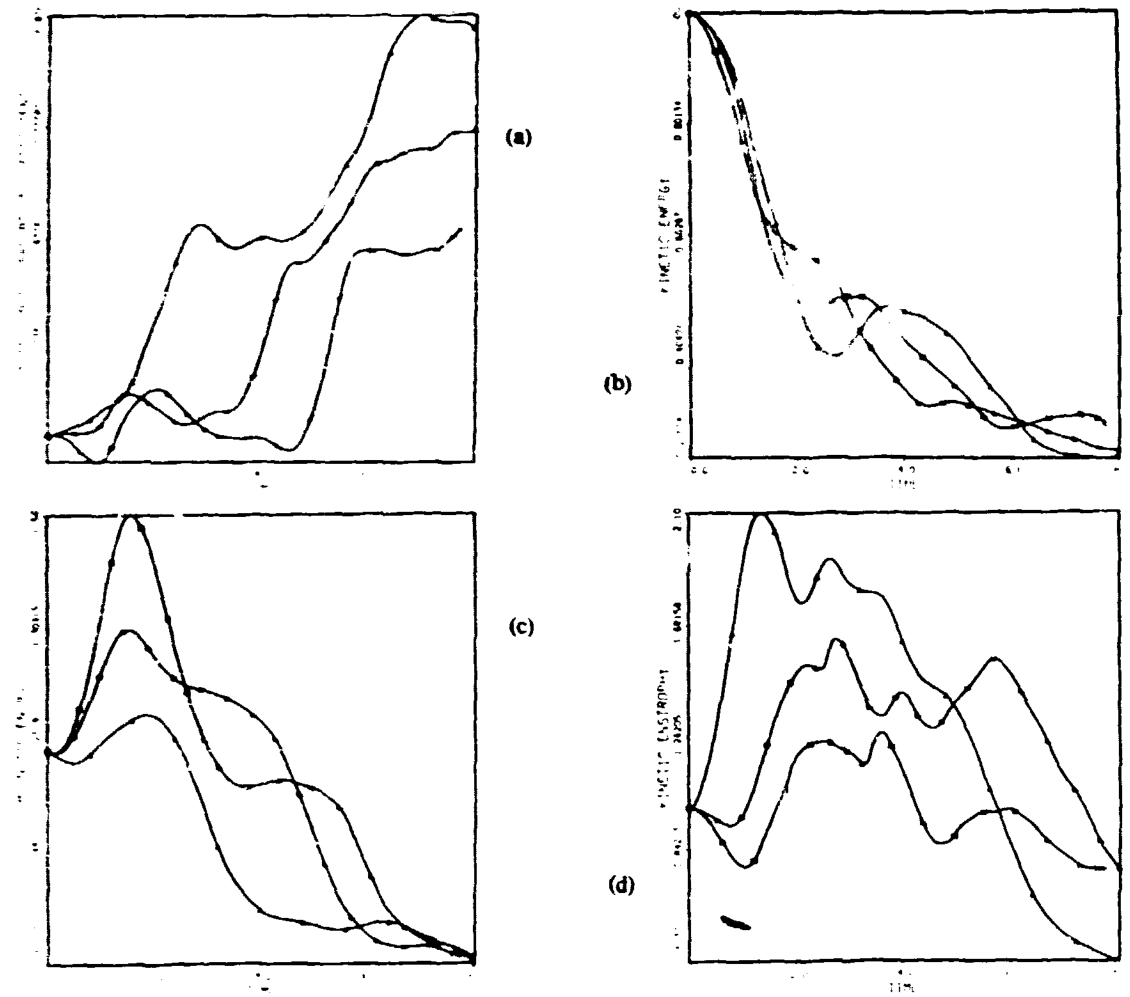

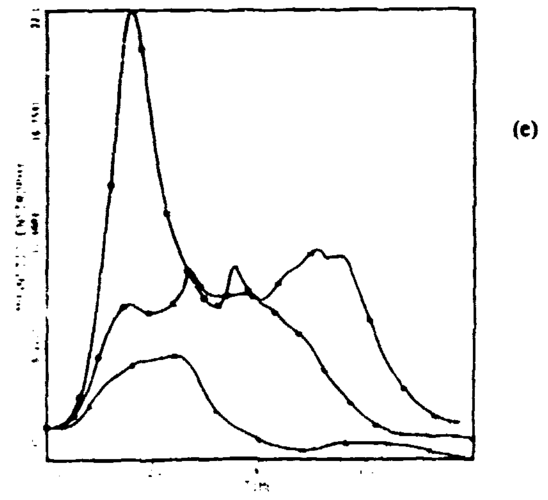

Fig. 8 — Evolution of global averages for S = 50 and M = 0.6 (Δ), M = 1.0 (○), and M = 1.5 (□). (a) Compressible correlation coefficient, α_c, (b) Kinetic energy, normalized to one at $t = 0$. (c) Magnetic energy. (d) Kinetic enstrophy, $\langle \omega^2 \rangle$. (e) Magnetic enstrophy, $\langle j^2 \rangle$.

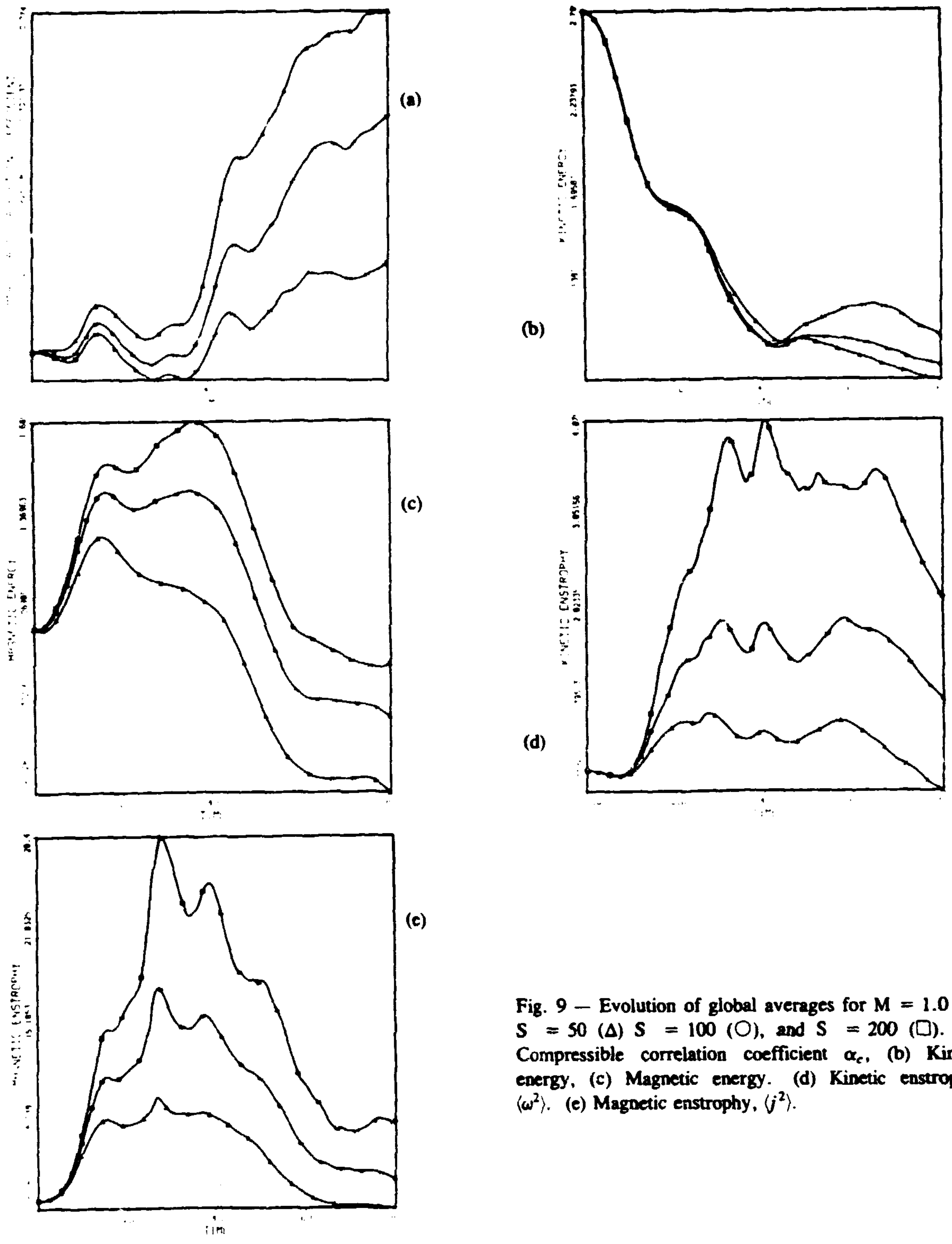

Fig. 9 — Evolution of global averages for M = 1.0 and S = 50 (Δ) S = 100 (○), and S = 200 (□). (a) Compressible correlation coefficient α_c, (b) Kinetic energy, (c) Magnetic energy. (d) Kinetic enstrophy, $\langle\omega^2\rangle$. (e) Magnetic enstrophy, $\langle j^2\rangle$.

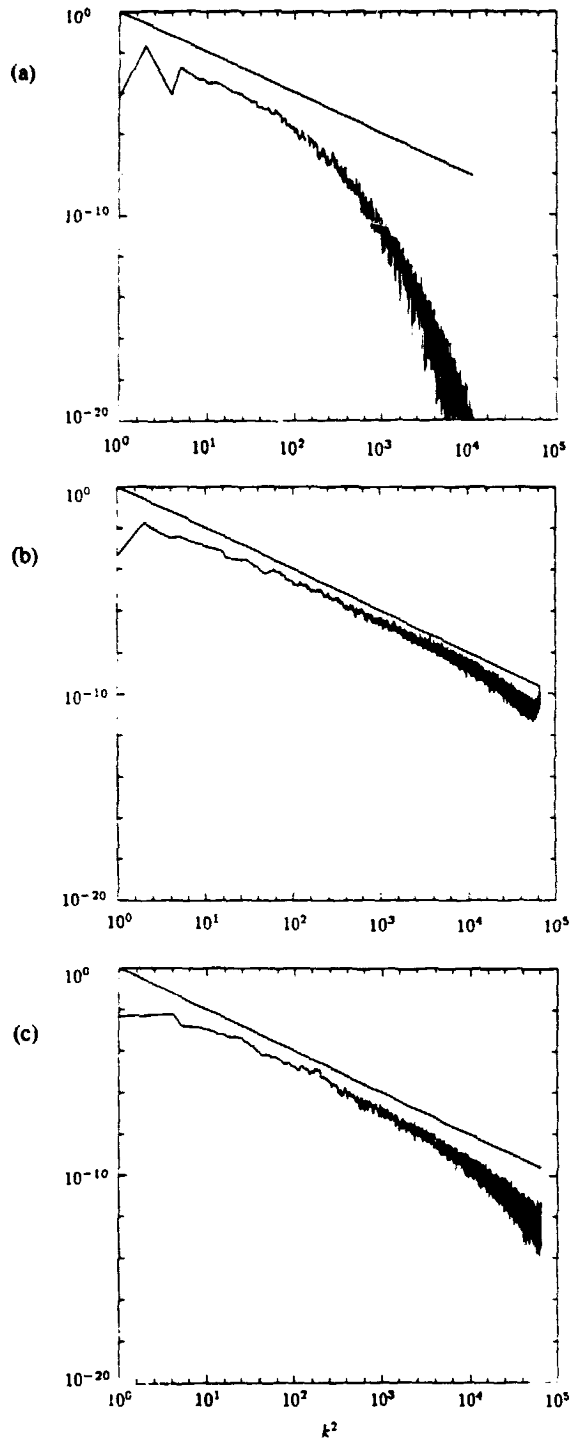

Fig. 10 — Autocorrelation spectra (log of magnitude squared) vs. log of squared wavenumber for (a) Mass density, $t = 1.0$, (b) Mass density, $t = 2.0$, (c) Mass density, $t = 4.0$, (d) Velocity, $t = 2.0$, (e) Nonsolenoidal component of the velocity, $t = 2.0$, (f) Solenoidal component of the velocity, $t = 2.0$, (g) magnetic field, $t = 2.0$.

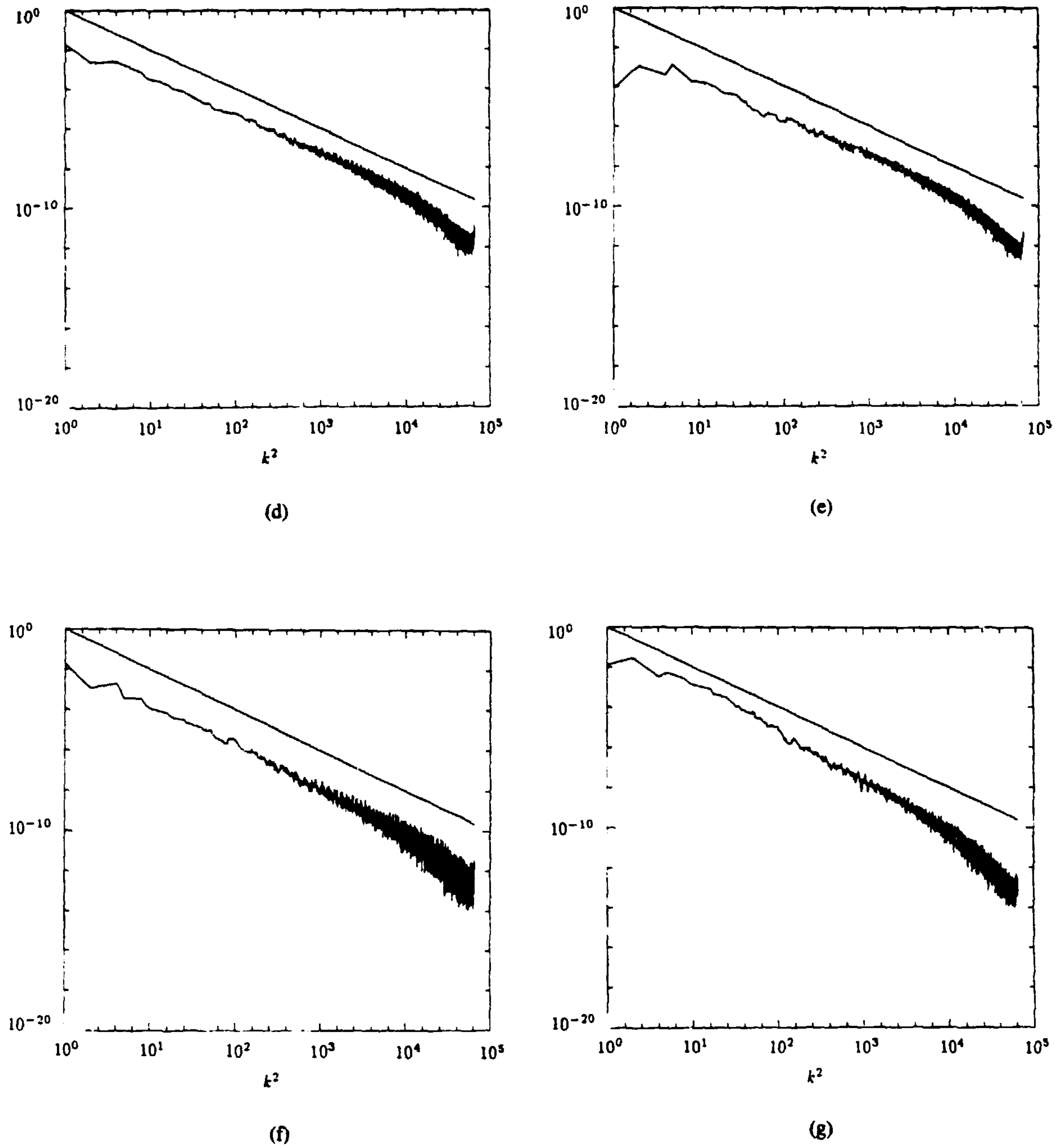

Fig. 10 — (Continued) Autocorrelation spectra (log of magnitude squared) vs. log of squared wavenumber for (a) Mass density, $t = 1.0$, (b) Mass density, $t = 2.0$, (c) Mass density, $t = 4.0$, (d) Velocity, $t = 2.0$, (e) Nonsolenoidal component of the velocity, $t = 2.0$, (f) Solenoidal component of the velocity, $t = 2.0$, (g) magnetic field, $t = 2.0$.

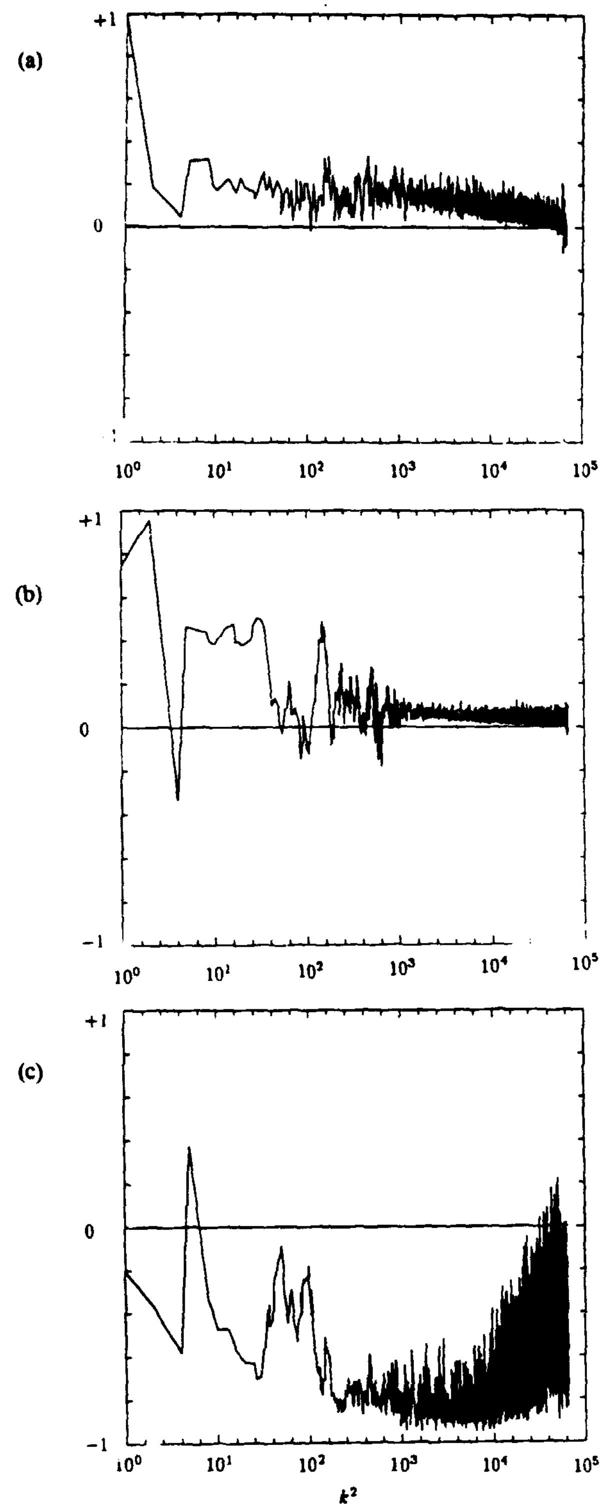

Fig. 11 — Normalized cross-correlation spectra vs. log of squared wavenumber. (a) Cross helicity $(2(\mathbf{v} \cdot \mathbf{B})(k)/(|\mathbf{v}|^2(k) + |\mathbf{B}|^2(k))$, $t = 2.0$. (b) cross helicity, $t = 6.0$. (c) Pressure and magnetic field, $t = 2.0$.